Interplay of charge density wave states and strain at the surface of $CeTe_2$

Bishnu Sharma,[1] Manoj Singh,[1] Burhan Ahmed,[1] Boning Yu,[1] Philip Walmsley,[2,3] Ian R. Fisher,[2,3] and Michael C. Boyer[1,*]

[1]*Department of Physics, Clark University, Worcester, Massachusetts 01610, USA*

[2]*Geballe Laboratory for Advanced Materials and Department of Applied Physics, Stanford University, Stanford, California 94305-4045, USA*

[3]*Stanford Institute for Materials and Energy Sciences, SLAC National Accelerator Laboratory, 2575 Sand Hill Road, Menlo Park, California 94025, USA*

(Received 15 November 2019; accepted 22 May 2020; published 17 June 2020)

We use scanning tunneling microscopy (STM) to study charge density wave (CDW) states in the rare-earth ditelluride, $CeTe_2$. Our STM measurements surprisingly detect a unidirectional CDW with $q \sim 0.28\,a^*$, which differs from previous experimental and first-principles studies of the rare-earth ditellurides, and which is very close to what is found in experimental measurements of the related rare-earth tritellurides. Furthermore, in the vicinity of an extended subsurface defect, we find spatially-separated as well as spatially-coexisting unidirectional CDWs at the surface of $CeTe_2$. We quantify the nanoscale strain and its variations induced by this defect, and establish a correlation between local lattice strain and the locally-established CDW states; this suggests that lattice strain plays an important role in determining the specific characteristics of the established CDW state. Our measurements probe the fundamental properties of a weakly-bound two-dimensional Te sheet, which experimental and theoretical work has previously established as the fundamental component driving much of the essential physics in both the rare-earth di- and tritelluride compounds.

DOI: 10.1103/PhysRevB.101.245423

I. INTRODUCTION

Charge density wave (CDW) states are found in numerous low-dimensional material systems where they coexist with other quantum orders such as superconductivity and magnetism. The interplay between elastic energy costs and electronic energy gains drives the details of a CDW state, characterized by charge localization, a periodic lattice distortion, and an energy gap in a material. Despite considerable progress in detailing these properties in a wide range of systems, fundamental questions persist. These questions range from determining the specifics of the driving mechanism for the CDW state within a given compound, to understanding the sensitivity of CDW states to parameters including elemental doping, external pressure, and strain.

Here we present our studies on $CeTe_2$, a member of the rare-earth ditelluride compounds (RTe_2 where R = rare-earth element). The RTe_2 compounds form in a Cu_2Sb-type tetragonal structure (space group $P4/nmm$) and comprise single Te square-planar sheets separated by rare-earth block layers [Fig. 1(a)]. The partially-filled in-plane $5p_x$ and $5p_y$ orbitals of the Te sheets allow for charge conduction within the a-b plane [1]. Separating each Te sheet is an insulating rare-earth block layer leading to a large out-of-plane resistivity and ultimately the quasi-two-dimensional nature of these materials. In $CeTe_2$, at room temperature, the CDW state is already well established, and the resistivity along the c-axis is ~40 to 100 times that along the in-plane resistivity [2,3].

First-principle calculations well approximate the Fermi surface of the RTe_2 compounds mapped by angle-resolved photoemission spectroscopy measurements [1,2,4–7], indicating the primary contributions of the $5p$ in-plane orbitals of the single Te square-planar sheets to the Fermi surface, and further illustrating the two-dimensional nature of these compounds. The parallel components of the Fermi surface indicate that the Fermi surface topology may be conducive to a Fermi-surface nesting-driven CDW occurring in the RTe_2 materials. Indeed, initial transmission electron microscopy (TEM) measurements [4] detected a superlattice structure with $q_{CDW} \sim \frac{1}{2}a^*$ in the $LaTe_2$ compound in agreement with the initially calculated Fermi-surface nesting vector [1,4]. However, subsequent x-ray measurements [8] find variations in the measured q_{CDW} including $q_{CDW} \sim \frac{1}{2}a^* + \frac{1}{2}b^*$ in $LaTe_2$, and TEM measurements [2] suggest a more complicated series of CDW wave vectors in $LaTe_2$ and the closely-related $CeTe_2$. Thus, the physics contained within these compounds is more-complex and less well understood than initially believed. Further, Lindhard susceptibility calculations evince a range of possible wave vectors which could nest the RTe_2 Fermi surface [2]. Hence, the specific CDW nesting wave vector established within an RTe_2 material may be affected by a number of factors, including the choice of rare-earth ion, lattice strain, and elemental vacancies (e.g., Te vacancies) which can both affect band filling as well as introduce local lattice strain. Furthermore, while Fermi-surface nesting has been identified as the primary candidate for the origin of the CDWs found in the RTe_2 compounds, we note that in the closely-related, and more intensely-studied RTe_3 compounds, the CDW-driving mechanism, initially suspected to be due to Fermi-surface nesting, is now of debate. Both

*Corresponding author: mboyer@clarku.edu

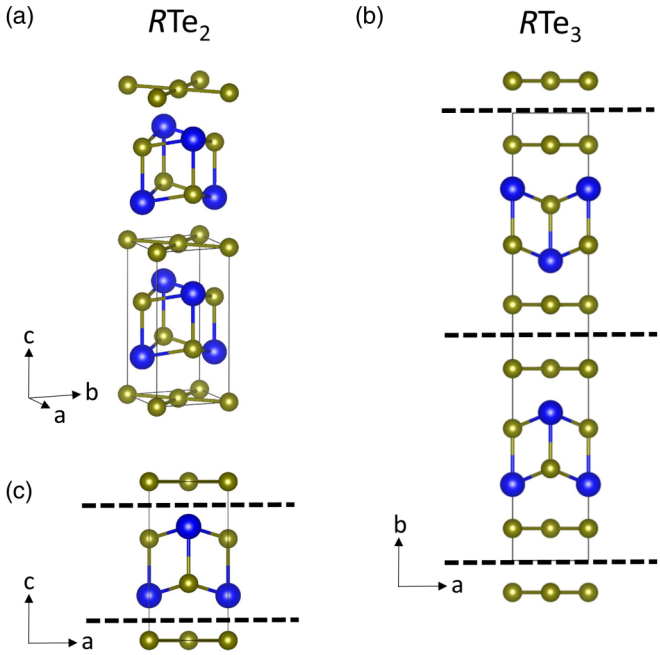

FIG. 1. Ions in gold color are Te ions. Ions in blue are rare-earth ions. (a) Crystal structure for $R\text{Te}_2$ compounds. (b) Crystal structure for $R\text{Te}_3$ compounds. Crystal cleave planes (dotted black lines) are between neighboring square-planar Te sheets. Cleaving the crystal exposes a square-planar Te sheet surface layer. (c) Two possible cleave planes (dotted black lines) for $R\text{Te}_2$. The top cleave plane would results in a surface rare-earth block layer. The bottom cleave plane would result in a surface Te sheet. Note the slightly different coordinate-axis conventions used for the $R\text{Te}_2$ and $R\text{Te}_3$ compounds. The crystal structures were constructed using VESTA software [29].

Fermi-surface nesting and electron-phonon coupling mechanisms, or a combination of the two, have been identified as possible candidates [9–15]. Given that considerably less attention has been given to the $R\text{Te}_2$ compounds, it is possible that the CDW-driving mechanism in these materials is not as clearly established as initially believed. Indeed, a strong electron-phonon coupling mechanism for the CDW in LaTe_2 compound has recently been suggested. [16]

To our knowledge, there have been no previous scanning tunneling microscopy (STM) measurements made on any member of the $R\text{Te}_2$ compounds. In this paper, we present our STM measurements on near-stoichiometric CeTe_2 single crystals. One goal of our studies is to image, in real space, the CDW state hosted by CeTe_2, and to compare our extracted q_{CDW} to those previously found in the $R\text{Te}_2$ compounds as well as to that found in the related $R\text{Te}_3$ compounds. Given the expected sensitivity of $R\text{Te}_2$ compounds to external factors such as strain [2,17], and given the demonstrated sensitivity of CDW states in $R\text{Te}_3$ to local [18,19] and global strain [15,20,21], a second goal is to provide a nanoscale view of the interplay of local lattice strain and the locally established CDW state(s) in CeTe_2.

II. EXPERIMENTAL METHODS

Single-crystal CeTe_2 samples were grown using a self-flux technique described in detail elsewhere [2]. The growth technique used effectively minimizes Te vacancies in the Te plane leading to near-stoichiometric samples. Unlike the $R\text{Te}_3$ compounds which easily cleave between the van der Waals bonded neighboring double-Te planes [Fig. 1(b)], the $R\text{Te}_2$ compounds cleave between the more tightly bound single Te plane and the neighboring block layer as seen in Fig. 1(c). An additional, but minor, consideration is that during the crystal growth process, a very thin surface layer of CeTe_3 grows on top of the CeTe_2 bulk crystal. To ensure removal of the CeTe_3 surface layer, we first cleave our CeTe_2 samples in ambient conditions using a razor blade or by mechanically striking a cleave post glued to the surface using silver epoxy. Subsequently, samples are inspected to ensure that the sample cleave occurred deep within the original sample before the sample is inserted into the vacuum chamber. Our scanning tunneling microscopy measurements were conducted at ∼300 K, a temperature at which CeTe_2 is already deep within the CDW state [2], and in ultrahigh vacuum ($\sim 10^{-9}$ Torr) using an RHK PanScan STM using a chemically etched tungsten tip. After chemical etching, the tungsten tip was annealed *in situ*, then sharpened through electron bombardment.

III. RESULTS AND DISCUSSION

A. Surface topography

Given that the crystal structure of CeTe_2 comprises repeating an alternating pattern of single Te layers and rare-earth block layers, it is expected that there is an equal possibility of exposing either as the surface layer upon cleaving. Unlike our previous work on the related TbTe_3 compound, we found it considerably more difficult to find large-scale, atomically flat regions on the exposed surfaces of CeTe_2. Often, our topographic images show a surface layer with small-scale step edges with hints of short-range atomic structure [Fig. 2(a)] rather than large-scale atomically flat regions with extended atomic structure which could be linked to the bulk crystal structure. The proliferation of step edges is likely due to the stronger bonding between neighboring layers within the $R\text{Te}_2$ compounds making cleaving more difficult; whereas $R\text{Te}_3$ compounds can easily be cleaved using tape, effective cleaving of CeTe_2 necessitates using a razor blade or mechanically hitting a cleave bar which is firmly fixed to the sample.

However, through large-scale scanning, we are indeed able to locate extensive, atomically flat regions for imaging and study. Figure 2(b) shows a typical topography acquired across an atomically flat region. Evident in the image are atomic periodicities over which a striped CDW pattern is superimposed. Figure 2(c) shows the fast Fourier transform (FFT) of such a typical topography, which evinces peaks which we can associate with the crystal lattice and established CDW state. We identify four peaks (circled in blue) associated with a square lattice and with a periodicity consistent with the CeTe_2 bulk lattice parameter of $a = 4.47$ Å reported by x-ray measurements [22]. Additionally, we identify four peaks (circled in orange) associated with a square lattice rotated 45° with respect to this first lattice, and with periodicity of $\frac{a}{\sqrt{2}}$. Following our previous work on the related TbTe_3 compound, where a near-identical FFT lattice peak layout is observed, we identify the peaks circled in orange as originating from the

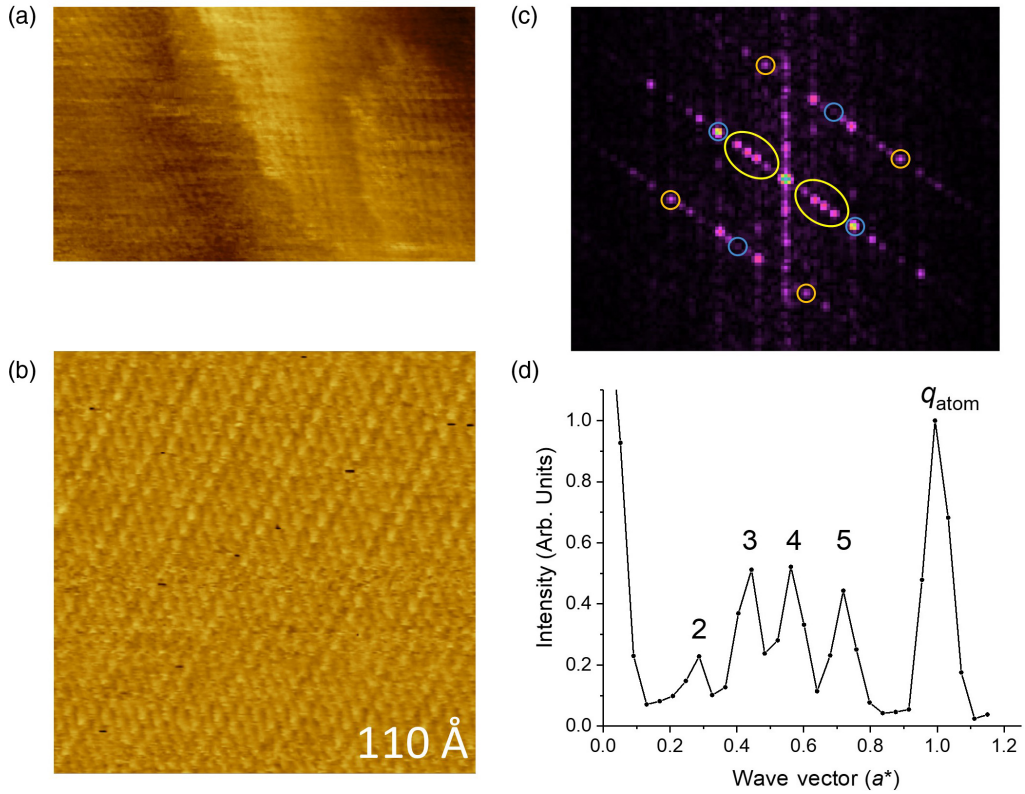

FIG. 2. (a) 100-Å×60-Å topographic image showing step edges as well as hints of atomic structure. The image was acquired with $V_{\text{sample}} = +500$ mV and $I = 200$ pA. (b) Typical topography in a flat region of the sample surface. The unidirectional CDW is seen in stripes superimposed on an atomic structure. The image was acquired with $V_{\text{sample}} = +200$ mV and $I = 400$ pA. (c) FFT of a typical topography. Orange circles enclose peaks originating from the surface square-planar Te sheet. Blue circles enclose peaks originating from the subsurface rare-earth block layer (Ce ions). Yellow ovals enclose four peaks associated with the unidirectional CDW and those originating from mixing between the CDW wave vector and the block-layer atomic wave vectors. (d) Linecut through the FFT in (c) beginning at the origin, in the direction of the CDW, and extending just past the atomic signal originating from the block layer (q_{atom}).

Te layer, and the peaks circled in blue as originating from the rare-earth block layer. In short, when scanning these regions in $CeTe_2$, as with the RTe_3 compounds, the tunneling current comprises contributions originating from both the Te and the rare-earth block layers. Previous STM work on the related $CeTe_3$ suggests that the signal from the rare-earth block layer is dominated by the Ce ion [23].

Furthermore, we identify four peaks (circled in yellow) associated with the striped CDW pattern. Figure 2(d) shows a linecut taken through the FFT starting at the origin, through these four CDW-associated peaks and extending past the block-layer peak. To extract the peak locations, we fit Gaussians to the peaks in Fig. 2(d), determining the four peak locations as 0.276 a^*, 0.434 a^*, 0.566 a^*, and 0.720 a^*, respectively, with estimated uncertainties extracted from the variance-covariance matrix of 0.006 a^*, 0.002 a^*, 0.002 a^*, and 0.002 a^*. These CDW-associated wave vectors are very close to those determined by STM measurements on the related RTe_3 compounds. Consequently, we label the peaks in Fig. 2(d) as "2," "3," "4," and "5," given that their wave-vector values are close to the $\sim 2/7$, $\sim 3/7$, $\sim 4/7$, and $\sim 5/7 q_{\text{atom}}$ CDW-associated wave vectors reported for STM measurements of the RTe_3 compounds [18,23,24]. Further, and following our previous work on $TbTe_3$, we identify peak 2 as the CDW wave vector, q_{CDW}, and peak 4 as the first harmonic, $2q_{\text{cdw}}$. Peaks 3 and 5 occur at $q_{\text{atom}} - 2q_{CDW}$ and $q_{\text{atom}} - q_{CDW}$, respectively, and we identify these peaks as resulting from wave-vector mixing, the nature of which is discussed in detail elsewhere [18,23,24]. As such, the origin of these four peaks is consistent with an incommensurate, unidirectional CDW established on the surface of $CeTe_2$.

Our identification of a unidirectional CDW in $CeTe_2$ is initially surprising. Previous TEM experiments report a considerably more complex CDW state in the bulk of $CeTe_2$ characterized by five wave vectors [2]. Even in the case of the related $LaTe_2$ where a unidirectional CDW was detected [4], the wave vector of $q_{CDW} \sim 0.50\ a^*$ noticeably differs from any of the four CDW-associated wave vectors we report. Rather, the origin of the four wave vectors can be understood in terms of the structural relation $CeTe_2$ has to the RTe_3 compounds and the fundamental physics contained within a single Te sheet. Cleaving an RTe_3 compound occurs between neighboring Te planes [Fig. 1(b)]; the exposed surface is a single Te plane which is directly above a rare-earth block layer. In contrast, cleaving an RTe_2 compound occurs between a single Te plane and a rare-earth block layer; this gives a 50% chance that the exposed surface is a single Te plane which is directly above a rare-earth block layer. In short, in the case that the RTe_2 compound cleaves such that the exposed surface is a Te plane, the STM tip probes a surface configuration which

is identical to that of the $R\mathrm{Te}_3$ compounds. Our previous work on TbTe_3 illustrates that the surface Te layer is only weakly bound to the bulk below and, as such, can host CDW states which differ from that observed in the bulk [18]. As a consequence, when the surface terminal layer is a Te plane, STM measurements probe the fundamental physics contained within a single Te plane, but the plane is subjected to outside influences such as local strain fields. Interestingly, while a weakly bound surface Te layer atop a block layer may appear physically similar for both the $R\mathrm{Te}_2$ and $R\mathrm{Te}_3$ compounds, one might still expect slightly different band fillings between the two [2] which would lead to differing Fermi surfaces. Given that the CDW wave vectors we detect in CeTe_2 are very close to those detected by STM in the $R\mathrm{Te}_3$ compounds, differences in band filling do not appear to significantly affect the detected CDW wave vectors. This may indicate that the observed CDW wave vectors are principally selected via a strongly momentum-dependent electron-phonon coupling rather than Fermi-surface nesting, connecting to other recent work [13,25].

Given that there is only a 50% chance of exposing a Te plane when cleaving an $R\mathrm{Te}_2$ compound, it is equally likely that a block layer will be exposed. If a block layer is exposed and if it is well coupled to the bulk below, then it is possible that probing the block layer with STM may give insight into the bulk CDW. However, the block layer is insulating since rare-earth ions in the block layer donate electrons to fill the p orbitals in the Te plane [1]. As a consequence, it is likely difficult to image this layer. Indeed, we have acquired numerous images of the CeTe_2 surface where neither large-scale (100s of nanometers) nor atomic-scale features are able to be resolved; this may be attributed to scanning a surface insulating block layer. When nanoscale features and atomic resolution are obtained, we detect a unidirectional CDW consistent with a surface Te layer. In none of our images, which include just under 5000 topographic images taken on multiple CeTe_2 crystals (as well as multiple cleaves), do we observe CDW wave vectors reflecting those previously reported in bulk studies of $R\mathrm{Te}_2$ compounds. Finally, while there is a propensity for Te vacancies to be introduced into the Te plane during the crystal growth process of $R\mathrm{Te}_2$ compounds [2], we do not typically observe atomic vacancies in our topographies. This appears to confirm the near-stoichiometric quality of our crystals.

B. Surface strain and CDW states

Properties of CDW states can be manipulated by straining a material. The application of external pressure or chemical pressure can strain a material's crystal lattice leading to changes in bulk-CDW transition temperatures as well as the emergence of other orders, including coexisting CDW states [20,21]. STM measurements are particularly useful in obtaining a local view of CDW states which, in turn, can be related to local lattice strain fields. For example, in NbSe_2, STM measurements have allowed for the identification of at least four different CDW orders which have been attributed to differing local lattice strain conditions [26,27]. In $1T$-TiSe_2, STM measurements show that Cu intercalation leads to the formation of striped CDW order instead of the typical 2×2 CDW order observed without intercalation; strain was suggested as a possible mechanism [28]. Our recent work on TbTe_3 [18] demonstrates that the material surface can host at least two distinct CDW states. In TbTe_3, these states can exist separately or coexist with one another. Furthermore, we suggested that the specific local CDW order may be tied to the local strain field induced onto the crystal surface when the sample is cleaved.

The topographic image in Fig. 3(a) was acquired over a 316-Å × 395-Å region of CeTe_2. Evident in the region, by eye, is a dominant unidirectional CDW state along the a_2 crystal axis in the lower left corner of the image, a dominant unidirectional CDW state along the a_1 axis in the upper right corner, and an apparent crossover region in between. While the in-plane axes of bulk CeTe_2 crystal structure are equivalent, here we label the axes as a_1 and a_2 so as to provide clarity in our analysis of the CDW states contained within this topographic region. Also prominent in this region, and possibly driving the observed CDW evolution across the region, is an extended subsurface defect of unknown origin leading to a hill-like feature with an apparent height of ∼3 nm, where the top right part of the surface of the image is higher than that in the flat region in the lower left corner. In the vicinity of this defect, it is important to emphasize that the surface layer is continuous throughout the imaged region; there are no breaks or step edges, leading to the conclusion that the defect is subsurface. As such, there is an evolution and coexistence of more than one CDW state within the imaged surface layer.

Fourier transforms of subregions denoted in red and blue in Fig. 3(b) confirm the multiple CDW states contained within the larger topographic region. The FFT of the red subregion [Fig. 3(c)], a region which extends across the hill-like defect and slightly beyond, shows evidence for CDWs established along both a_1 and a_2 crystal axes. The FFT of the blue subregion [Fig. 3(d)], a region which is primarily in an atomically flat region and extends only minimally onto the defect, shows a CDW predominately along the a_2 axis within the region. In particular, the FFT in Fig. 3(d) strongly resembles that seen for a typical topography in Fig. 2(c). In both FFTs, peaks can be contributed to Te ions, Ce ions from the rare-earth layer, and to a unidirectional CDW; this is consistent with probing a Te layer on top of a block layer in the regions imaged in Fig. 3. Given the obvious spatial variation in the CDW states hosted in this topographic region, we are led to the following questions: (1) How does the lattice evolve across the region? (2) How do the CDW states evolve across the region? (3) Is there a correlation between the lattice evolution and the locally established CDWs?

To address these questions, we subdivide the large topographic image into twenty 79-Å×79-Å square regions [white squares in Fig. 3(b)] and analyze each. Taking Fourier transforms of each allows for the determination of the associated local average lattice parameters and CDW wave vectors. Whereas in our previous work we used the surface Te ion locations to determine the lattice parameters in the Te surface layer of TbTe_3, here we use the slightly more prominent subsurface-originating Ce (block-layer) peaks in the FFTs so as to extract the local lattice parameters. The lattice parameters were extracted by fitting Gaussians to the two Ce ion-associated peaks in each region's FFT to determine their associated wave vectors. As shown previously, due to the STM tip condition

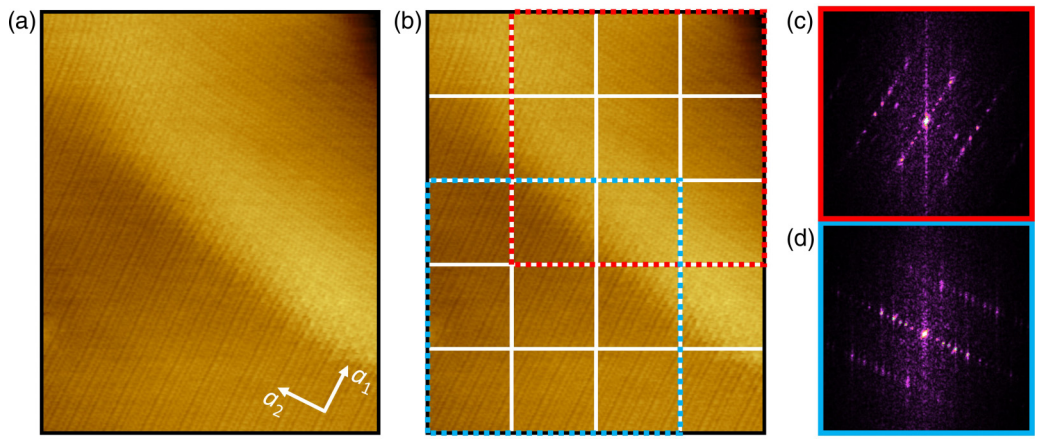

FIG. 3. (a) 316-Å×395-Å topographic image showing two unidirectional CDWs, a crossover region where the two CDWs coexist, and an extended subsurface defect. The image was acquired with $V_{\text{sample}} = +150$ mV and $I = 500$ pA. (b) The topographic image in (a) is split into twenty 79-Å × 79-Å subregions (white squares). Analysis of each of these subregions allows for a more-local understanding of the CDW states, local lattice parameters, and possible correlations between the two. (c) FFT of region of (b) enclosed by the red-dotted square. This region extends over much of the subsurface defect and shows evidence for CDW states along both the a_1 and a_2 axes, in addition to atomic periodicities associated with both the Te layer and rare-earth block layer. (d) FFT of region of (b) enclosed by the blue-dotted square. This region is primarily in the atomically flat region of the topographic image but its corner extends into the defect-affected area. Here only a unidirectional CDW state along the a_2 axis is obvious by eye. This FFT resembles the FFT in Fig. 2(c) for that of a typical surface region on $CeTe_2$.

and/or variations in the coupling of the top Te layer to the block layer below, the intensity of the block-layer (Ce) peaks in the FFT can be greater than those of the Te layer, even if the Te layer is closest to the STM tip [18]. Furthermore, the ∼1% smaller average lattice parameter in the Te layer [compared to the bulk lattice parameter found in $TbTe_3$ [18]] is insignificant as compared to the extreme lattice parameter variations found in this region of $CeTe_2$. Consequently, the use of the subsurface Ce ions to determine the local lattice parameter is a good reflection of the lattice parameters and their variations, for the directly imaged surface Te layer.

Plots in Figs. 4(a) and 4(b) show the average a_1 and a_2 lattice parameters for each of the 20 square subregions and provide a visualization of the spatial variation for each and a connection to local strain. Both plots show localized regions with average lattice parameters which differ from that in the bulk, but the a_1 lattice parameter has a much stronger spatial variation, ranging from a minimum of 3.90 Å (13% compressive strain) to a maximum of 5.41 Å (21% tensile strain), than that of a_2, ranging from a minimum of 4.45 Å (∼bulk value) to a maximum of 4.88 Å (9% tensile strain). Further, there is a clear spatial evolution to the lattice parameters where, on average, both a_1 and a_2 lattice parameters are smaller in the flat lower left of the region of Fig. 3(a) compared to the defect region in the upper right. Importantly, we note that we have acquired multiple images (over 120) spanning several days directly in, and in close proximity to, the area shown in Fig. 3(a). Analysis of these images gives results consistent with those presented in this paper, thereby allowing us to eliminate piezohysteresis and temperature drift as possible causes of the strain variations detected. The subsurface defect introduces significant lattice strain, leading to an expansion of both lattice parameters in the defect-affected region. In short, the topographic region in Fig. 3(a) provides an opportunity in which to study the nanoscale interplay of compressive and tensile strain and the locally established CDW states in $CeTe_2$.

Figure 4(c) shows the ratio of the a_1 to the a_2 lattice parameter for each of the 20 subregions. Superimposed on top of this plot are two black dotted lines separating three distinct CDW regions. In the lower left region, where a_1/a_2 is always less than 1, only CDW peaks along the a_2^* axis are observed in FFTs of the subregions (no CDW peaks along the a_1^* axis are observed above the noise level); this region has a unidirectional CDW established along the a_2 axis. In the upper right region, where a_1/a_2 is always greater than 1, only CDW peaks along the a_1^* direction are detected; this region has a unidirectional CDW established along the a_1 axis. In the middle region, where neither a_1 nor a_2 is consistently larger throughout, CDW peaks are observed along both the a_1^* and a_2^* directions; this region is a crossover region where both unidirectional CDWs coexist.

The local evolution of the CDW states across these three regions correlates with the spatial evolution of the lattice strain. In the lower left region, there is compressive strain along the a_1 axis whereas the a_2 lattice parameter is close to that of the bulk. Throughout this region the a_1 lattice parameter is smaller than that of the a_2 lattice parameter, and a CDW state purely along the a_2 axis is established. In the upper right region, there is tensile strain along both the a_1 and a_2 axes; however, the tensile strain along the a_1 axis is larger, leading to a_1 lattice parameters which are larger than a_2 throughout the region. Within this region, only a unidirectional CDW along the a_1 axis is established. Finally, the middle region is a crossover region where both CDWs coexist, and neither the a_1 lattice parameter nor the a_2 lattice parameter is consistently larger. A clear correlation appears between strain along the a_1 and a_2 axes and the established CDW states.

Next, we examine the local wave vectors, q_{CDW1} and q_{CDW2}, associated with the CDW states established along the

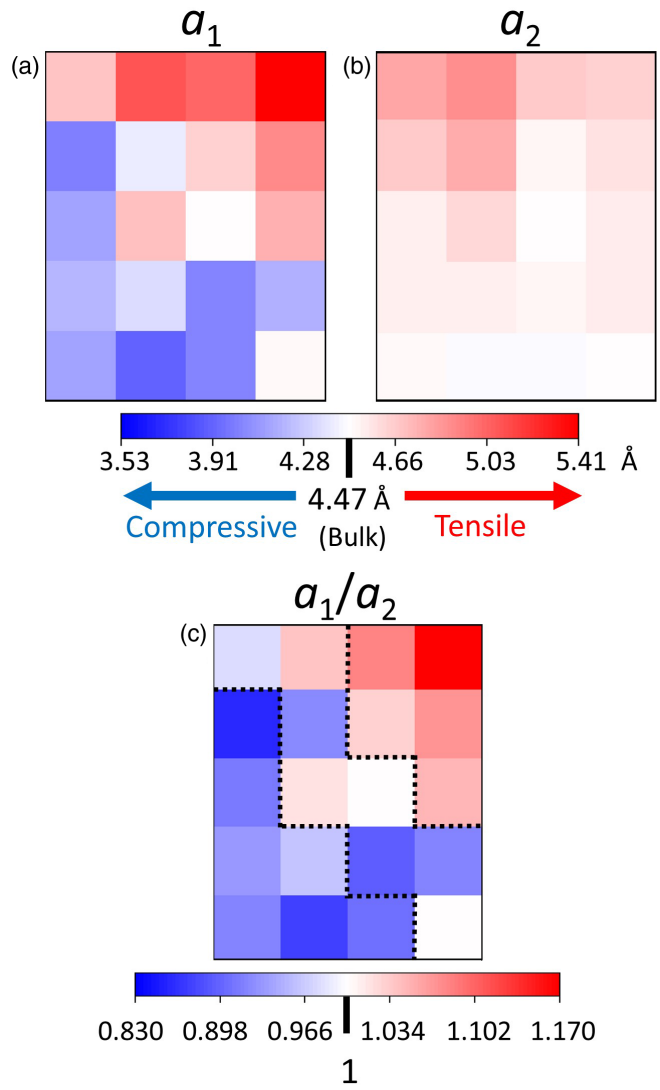

FIG. 4. (a) Plot of the a_1 lattice parameter for each of the 20 subregions of Fig. 3(b). There is a strong spatial variation in the a_1 lattice parameter across the full region. In the atomically flat region, the lattice parameter is lower than that in the bulk, indicating compressive strain. In the defect-affected region, the a_1 lattice parameter becomes significantly larger than that of bulk, indicating tensile strain. b) Plot of the a_2 lattice parameter for each of the 20 subregions of Fig. 3(b). The a_2 lattice parameter shows less variation across the topographic region than does the a_1 lattice parameter. However, in the defect-affected area, the a_2 lattice parameter becomes larger than that for the bulk, indicating tensile strain. (c) Plot of the ratio of the two lattice parameters (a_1/a_2) for each of the 20 subregions. Dotted lines are superimposed on the plot to indicate three regions. The lower left corner, where a_1/a_2 is always less than 1, hosts only a unidirectional CDW along the a_2 axis. The upper right corner, where a_1/a_2 is always greater than 1, is a region where there is only a unidirectional CDW along the a_1 axis. The region in between is a crossover region where both unidirectional CDWs coexist, and neither the a_1 nor a_2 local lattice parameter is consistently larger throughout this region.

a_1 and a_2 axes, respectively, for each of the 20 subregions [Figs. 5(a) and 5(b)]. The regions in gray indicate the absence of the CDW along that direction; any CDW-associated peak in the FFT is within the noise level. In Fig. 5, q_{CDW1} and q_{CDW2}

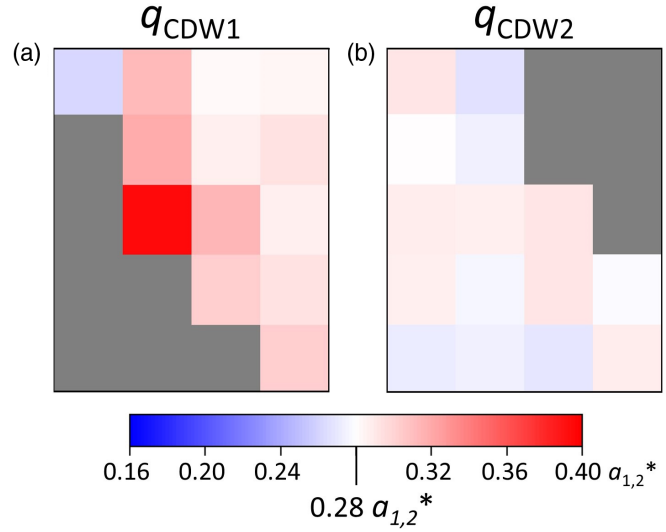

FIG. 5. (a) Plot of the wave vector for the unidirectional CDW along the a_1 axis (q_{CDW1}) for each of the 20 subregions. The gray region of the plot indicates a region where any signal associated with the a_1 axis CDW is absent (within the noise level). q_{CDW1} and q_{CDW2} (b) are expressed in terms of the locally associated a_1^* and a_2^* for an individual subregion. (b) Plot of the wave vector for the unidirectional CDW along a_2 axis (q_{CDW2}) for each of the 20 subregions. The CDW along the a_2 axis is absent in the gray region.

are expressed in terms of the locally associated a_1^* and a_2^* for an individual subregion. In the region in Fig. 2(b), away from any obvious defects, $q_{CDW} = 0.28\,a^*$. Note that if the local CDW wave vectors within a given subregion were pinned to the average local lattice parameter, the plots in Figs. 5(a) and 5(b) would show a single white color throughout, indicating that the CDW wave vectors directly mimic changes

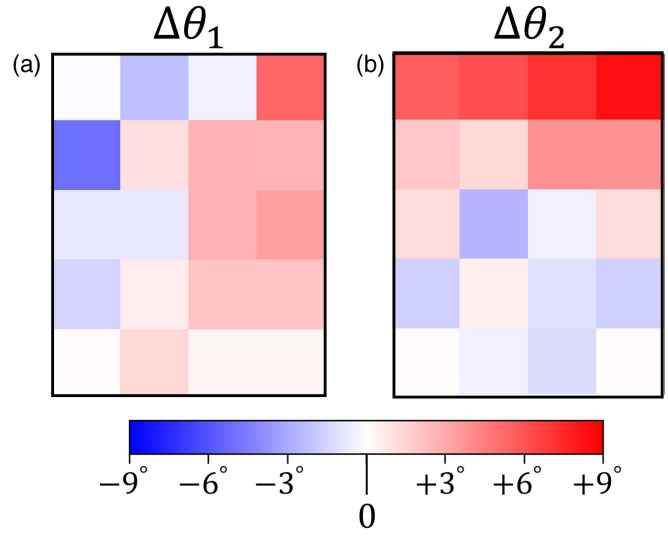

FIG. 6. (a) Angular rotation of the a_1 lattice parameter for each of the 20 subregions relative to its orientation in the subregion in the lower left corner of the plot. "+" represents a counterclockwise rotation and "–" represents a clockwise rotation. (b) Angular rotation of a_2 lattice parameter as compared to its orientation in the subregion in the lower left corner of the plot.

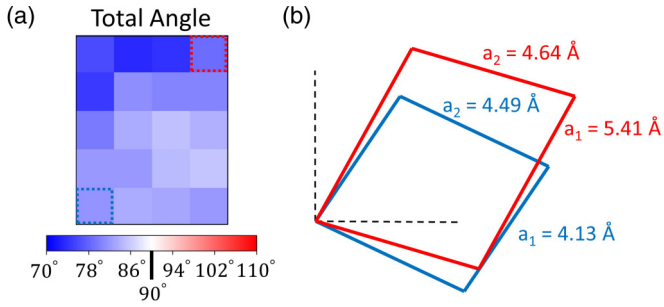

FIG. 7. (a) Plot of the total angle between the a_1 and a_2 lattice parameters for each of the 20 subregions. (b) Shown in blue is the unit cell for the blue-dotted region in (a). Here $a_1 < a_2$, and there is a CDW only along the a_2 axis. In red, the unit cell for the red-dotted region in (a) is drawn preserving the scale and orientation relative to the blue unit cell. In this subregion, $a_1 > a_2$ there is a CDW only along the a_1 axis.

to the average lattice parameter from one region to the next. Instead, we find variations for each. Throughout the region, $q_{\mathrm{CDW}2}$ shows relatively small variations ($\sim 0.27 - 0.29\, a_2^*$) as compared to $q_{\mathrm{CDW}1}$. $q_{CDW\,1}$ ranges from $0.28 - 0.29\, a_1^*$ in the upper right region in which there is only a CDW along the a_1 axis. Within the crossover region, $q_{CDW\,1}$ varies significantly with a minimum of $0.26\ a_1^*$ in the top leftmost corner and a maximum of $0.40\ a_1^*$ near center. In general, in regions where there is only a single unidirectional state present, $q_{CDW\,1,2}$, is close to the $0.28\ a^*$ found in regions away from defects. In the crossover region, there are stronger variations in $q_{CDW\,1,2}$, although the CDW states remain collinear with the a_1 and a_2 axes across the entire topographic region.

As is evident in the top left of Fig. 3(a), the two unidirectional CDW states established in the region do not appear perpendicular to one another throughout, and appear, at some locations, to be rotated relative to crystal axes drawn as a guide on the figure. However, these drawn crystal axes are slightly misleading as the lattice unit cell changes throughout the region; the local a_1 and a_2 axes not only expand/contract, but also slightly rotate from one region to the next, as seen in Figs. 6(a) and 6(b). Figure 7(a) shows the *relative* angle between the a_1 and a_2 axes for each subregion. For each subregion the relative angle between the a_1 and a_2 axes is smaller than 90°, ranging from a minimum of 73° to a maximum of 85°. Together, this indicates that in addition to compressive and tensile strain throughout the region, there is also lattice shear strain. This lattice shear strain affects the local CDW state by causing a rotation of the CDW wave vectors; the CDW remains collinear with the average local a_1 and a_2 axes for each of the subregions.

Figure 7(b) provides a visual illustration of the average unit cells for the two subregions of Fig. 7(a) enclosed by dotted squares, and helps to highlight some of the longitudinal and rotational changes to the a_1 and a_2 axes as well as the unit cell which occur in the region. The first subregion [dotted dark-blue square of Fig. 7(a)] is in a region where there is purely a unidirectional CDW along the local a_2 axis; here the lattice parameters are such that $a_2 > a_1$. The second subregion [dotted red square in Fig. 7(a)] is in a region where there is only a unidirectional CDW along the a_1 axis; here $a_1 > a_2$. The unit cells are drawn so as to preserve their relative scale and are oriented with respect to the x- and y-image scan directions. The rotation of the local a_1 and a_2 axes (e.g., unit cell) is clear, as is the $\sim 3^\circ$ relative angular change between the axes in the two regions.

IV. CONCLUSIONS

We have acquired STM measurements on $CeTe_2$, a member of the RTe_2 compounds. In contrast to bulk measurements, we observe a unidirectional CDW with a wave vector very similar to that found in the RTe_3 compounds. This correspondence can be understood in terms of STM measurements directly probing a Te surface layer which is weakly bound to the rare-earth block layer below for each compound. Much of the essential physics within the R-Te compounds can be captured using a model of a single square Te plane [4,11,12]. As a consequence, our STM measurements probe the essential physics contained within this plane which is subject to weak coupling to the block layer and to lattice strain induced by defects. Our measurements suggest that the CDW wave vectors we observe in $CeTe_2$ may be determined by a strongly momentum-dependent electron-phonon coupling. In $NbSe_2$, where the CDW states are similarly believed driven by an electron-phonon coupling mechanism, previous work combining STM measurements with tight-binding modeling indicates that lattice strain (1) modifies phonon dispersions (affecting soft modes) and (2) modifies the strength of the electron-hopping parameters [27]. Similar considerations may be at play in $CeTe_2$. By studying changes in the lattice parameters and CDW states in the vicinity of an extended defect, we find a correlation between nanoscale lattice strain and locally-established CDW states.

ACKNOWLEDGMENTS

Scanning tunneling microscopy studies at Clark University were supported by the National Science Foundation under Grant No. DMR-1904918. Crystal growth and characterization at Stanford University (P.W. and I.R.F.) was supported by the Department of Energy, Office of Basic Energy Sciences under Contract No. DE-AC02-76SF00515.

[1] A. Kikuchi, Electronic structure of lanthan ditellurides, J. Phys. Soc. Jpn. **67**, 1308 (1998).

[2] K. Y. Shin, V. Brouet, N. Ru, Z. X. Shen, and I. R. Fisher, Electronic structure and charge-density wave formation in $LaTe_{1.95}$ and $CeTe_{2.00}$, Phys. Rev. B **72**, 085132 (2005).

[3] B. H. Min, E. D. Moon, H. J. Im, S. O. Hong, Y. S. Kwon, D. L. Kim, and H. C. Ri, Transport properties in low carrier system CeTe2, Phys. B: Condens. Matter **312–313**, 205 (2002).

[4] E. DiMasi, B. Foran, M. C. Aronson, and S. Lee, Stability of charge-density waves under continuous variation of band

filling in $LaTe_{2-x}Sb_x$ ($0 \leqslant x \leqslant 1$), Phys. Rev. B **54**, 13587 (1996).

[5] J. H. Shim, J. S. Kang, and B. I. Min, Electronic Structures of RTe_2 (R = La,Ce): A Clue to the Pressure-Induced Superconductivity in $CeTe_{1.82}$, Phys. Rev. Lett. **93**, 156406 (2004).

[6] E. Lee, D. H. Kim, J. D. Denlinger, J. Kim, K. Kim, B. I. Min, B. H. Min, Y. S. Kwon, and J. S. Kang, Angle-resolved and resonant photoemission spectroscopy study of the Fermi surface reconstruction in the charge density wave systems $CeTe_2$ and $PrTe_2$, Phys. Rev. B **91**, 125137 (2015).

[7] E. Lee, H. W. Kim, S. Seong, J. D. Denlinger, Y. S. Kwon, and J. S. Kang, Soft X-ray synchrotron radiation spectroscopy study of rare-earth chalcogenide charge-density wave compounds, J. Korean Phys. Soc. **70**, 389 (2017).

[8] K. Stöwe, Crystal structure and electronic band structure of LaTe2, J. Solid State Chem. **149**, 155 (2000).

[9] R. G. Moore, V. Brouet, R. He, D. H. Lu, N. Ru, J. H. Chu, I. R. Fisher, and Z. X. Shen, Fermi surface evolution across multiple charge density wave transitions in $ErTe_3$, Phys. Rev. B **81**, 073102 (2010).

[10] J. Laverock, S. B. Dugdale, Z. Major, M. A. Alam, N. Ru, I. R. Fisher, G. Santi, and E. Bruno, Fermi surface nesting and charge-density wave formation in rare-earth tritellurides, Phys. Rev. B **71**, 085114 (2005).

[11] E. DiMasi, M. C. Aronson, J. F. Mansfield, B. Foran, and S. Lee, Chemical pressure and charge-density waves in rare-earth tritellurides, Phys. Rev. B **52**, 14516 (1995).

[12] H. Yao, J. A. Robertson, E.-A. Kim, and S. A. Kivelson, Theory of stripes in quasi-two-dimensional rare-earth tellurides, Phys. Rev. B **74**, 245126 (2006).

[13] M. Maschek, S. Rosenkranz, R. Heid, A. H. Said, P. Giraldo-Gallo, I. R. Fisher, and F. Weber, Wave-vector-dependent electron-phonon coupling and the charge-density-wave transition in $TbTe_3$, Phys. Rev. B **91**, 235146 (2015).

[14] H.-M. Eiter, M. Lavagnini, R. Hackl, E. A. Nowadnick, A. F. Kemper, T. P. Devereaux, J.-H. Chu, J. G. Analytis, I. R. Fisher, and L. Degiorgi, Alternative route to charge density wave formation in multiband systems, Proc. Natl. Acad. Sci. USA **110**, 64 (2013).

[15] R. G. Moore, W. S. Lee, P. S. Kirchman, Y. D. Chuang, A. F. Kemper, M. Trigo, L. Patthey, D. H. Lu, O. Krupin, M. Yi, D. A. Reis, D. Doering, P. Denes, W. F. Schlotter, J. J. Turner, G. Hays, P. Hering, T. Benson, J. H. Chu, T. P. Devereaux, I. R. Fisher, Z. Hussain, and Z. X. Shen, Ultrafast resonant soft x-ray diffraction dynamics of the charge density wave in $TbTe_3$, Phys. Rev. B **93**, 024304 (2016).

[16] H. X. Yang, Y. Cai, C. Ma, J. Li, Y. J. Long, G. F. Chen, H. F. Tian, L. L. Wei, and J. Q. Li, Direct imaging of incommensurate wave pockets in the charge-density-wave state of LaTe2, EPL **114**, 67002 (2016).

[17] M. Lavagnini, A. Sacchetti, L. Degiorgi, E. Arcangeletti, L. Baldassarre, P. Postorino, S. Lupi, A. Perucchi, K. Y. Shin, and I. R. Fisher, Pressure dependence of the optical properties of the charge-density-wave compound $LaTe_2$, Phys. Rev. B **77**, 165132 (2008).

[18] L. Fu, A. M. Kraft, B. Sharma, M. Singh, P. Walmsley, I. R. Fisher, and M. C. Boyer, Multiple charge density wave states at the surface of $TbTe_3$, Phys. Rev. B **94**, 205101 (2016).

[19] A. Fang, J. A. W. Straquadine, I. R. Fisher, S. A. Kivelson, and A. Kapitulnik, Disorder induced suppression of CDW long range order: STM study of Pd-intercalated $ErTe_3$, Phys. Rev. B **100**, 235446 (2019).

[20] N. Ru, C. L. Condron, G. Y. Margulis, K. Y. Shin, J. Laverock, S. G. Dugdale, M. F. Toney, and I. R. Fisher, Effect of chemical pressure on the charge density wave transition in rare-earth tritellurides RTe_3, Phys. Rev. B **77**, 035114 (2008).

[21] D. A. Zocco, J. J. Hamlin, K. Grube, J. H. Chu, H. H. Kuo, I. R. Fisher, and M. B. Maple, Pressure dependence of the charge-density-wave and superconducting states in $GdTe_3$, $TbTe_3$, and $DyTe_3$, Phys. Rev. B **91**, 205114 (2015).

[22] M. H. Jung, K. Umeo, T. Fujita, and T. Takabatake, Competing interactions and anisotropic magnetoresistance in layered $CeTe_2$, Phys. Rev. B **62**, 11609 (2000).

[23] A. Tomic, Z. Rak, J. P. Veazey, C. D. Malliakas, S. D. Mahanti, M. G. Kanatzidis, and S. H. Tessmer, Scanning tunneling microscopy study of the $CeTe_3$ charge density wave, Phys. Rev. B **79**, 085422 (2009).

[24] A. Fang, N. Ru, I. R. Fisher, and A. Kapitulnik, STM Studies of $TbTe_3$: Evidence for a Fully Incommensurate Charge Density Wave, Phys. Rev. Lett. **99**, 046401 (2007).

[25] M. D. Johannes and I. I. Mazin, Fermi surface nesting and the origin of charge density waves in metals, Phys. Rev. B **77**, 165135 (2008).

[26] A. Soumyanarayanan, M. M. Yee, Y. He, J. van Wezel, D. J. Rahn, K. Rossnagel, E. W. Hudson, M. R. Norman, and J. E. Hoffman, Quantum phase transition from triangular to stripe charge order in $NbSe_2$, Proc. Natl. Acad. Sci. USA **110**, 1623 (2013).

[27] S. Gao, F. Flicker, R. Sankar, H. Zhao, Z. Ren, B. Rachmilowitz, S. Balachandar, F. Chou, K. S. Burch, Z. Wang, J. van Wezel, and I. Zeljkovic, Atomic-scale strain manipulation of a charge density wave, Proc. Natl. Acad. Sci. USA **115**, 6986 (2018).

[28] A. M. Novello, M. Spera, A. Scarfato, A. Ubaldini, E. Giannini, D. R. Bowler, and C. Renner, Stripe and Short Range Order in the Charge Density Wave of 1T-Cu_xTiSe_2, Phys. Rev. Lett. **118**, 017002 (2017).

[29] K. Momma and F. Izumi, VESTA 3 for three-dimensional visualization of crystal, volumetric and morphology data, J. Appl. Crystallogr. **44**, 1272 (2011).